Aggregation of *N*-Heteropolycyclic Aromatic Molecules: The Acridine Dimer and Trimer

Stefan Germer,[a] Marco Bauer,[b] Olaf Hübner,[a] Andreas Dreuw,[b] Hans-Jörg Himmel*[a]

Polycyclic aromatic hydrocarbons and their nitrogen-substituted analogues are of great interest for various applications in organic electronics. The performance of such devices is determined not only by the properties of the single molecules, but also by the structure of their aggregates, which often form via self-aggregation. Gaining insight into such aggregation processes is a challenging task, but crucial for a fine-tuning of the materials properties. In this work, an efficient approach for the generation and characterisation of aggregates is described, based on matrix-isolation experiments and quantum-chemical calculations. This approach is exemplified for aggregation of acridine. The acridine dimer and trimer are thoroughly analysed on the basis of matrix-isolation spectroscopy over two spectral ranges and quantum chemical calculations, which agree well with each other. Thereby a novel structure of the acridine dimer is found, which disagrees with a previously reported one. In addition, a structure of the trimer is determined and new insight into the photophysics of small acridine aggregates is gained. Finally, an outlook is given on how even higher aggregates can be made accessible through experiment.

Introduction

The interactions between two or more aromatic molecules are of fundamental interest since they can lead to the intercalation of polycyclic aromatic hydrocarbons into DNA,[1] influence supra-molecular structures[2] and determine the conductivity of polycyclic aromatic hydrocarbons and their corresponding *N*-hetero polycycles (NHPs), which are used in organic electronics.[3] The structure of such interacting aromatic molecules has been the subject of several theoretical studies, including those on dimers of benzene,[4] naphthalene[5] and anthracene.[6]

An experimental way to generate and investigate dimers and other small aggregates is supersonic jet spectroscopy.[7] Here, supersonic expansions are probed for aggregates using techniques like laser-induced fluorescence or multiphoton ionisation. Such studies have been conducted for the systems listed above[8–10], but also for nitrogen-containing aromatic molecules like imidazole,[11] pyrrole[12], pyridine[13] and phenanthrenes.[14] Mainly dimers were observed, but in a few studies, such as those of imidazole[11] and naphthalene,[15] even trimers were clearly identified.

The matrix-isolation spectroscopy is another experimental method used to selectively generate and analyse small aggregates. The matrices can be obtained by condensing the molecules with neon from the gas phase onto an inert surface cooled to 4 K. These molecules are thus statistically incorporated at defect sites of the polycrystalline solid Ne host. The occurrence of aggregates can be controlled by adjusting the ratio between the deposited amounts of molecules and Ne. Annealing a Ne matrix to 10 K allows the guest molecules to move and form further aggregates after deposition. Such matrices are stable for days and can be analysed using standard absorption spectroscopy methods. Even large molecules, which are difficult to accumulate in the gas phase, can be studied by the matrix-isolation technique, as has been shown in various works.[16–20] In terms of aggregates, this enabled us not only to characterise matrix-isolated pyridine dimers[21] in more detail compared to previous findings from supersonic jet spectroscopy,[13] but also to investigate matrix-isolated dimers of larger polycyclic aromatic hydrocarbons and their corresponding NHPs, such as tetracene, pentacene and some of their *N*-substituted derivatives.[22,23] Higher aggregates are rarely described. The latter was achieved, for instance, with the monocyclic pyrrole isolated in Ne matrices, where trimers were identified on the basis of the IR absorption shift of its NH stretching mode.[12] Furthermore, we were able to observe trimers of the polycyclic compounds benzo[*a*]- and benzo[*c*]acridine next to dimers and monomers based on their red-shifted electronic absorption in Ne matrices as well.[24] However, the signals were weak and the assignments were made tentatively.

Acridine (ACR) is another member of the NHP family (Figure 1). Its monomer and dimer spectra have been investigated by both matrix-isolation and supersonic jet spectroscopy. Absorption and emission spectra of excited singlet and triplet states were measured in solid hydrocarbon[25–27] and Ar[28–30] matrices at cryogenic temperatures. IR spectra of monomers in Ar matrices were obtained as well.[31] Electronic emission signals of dimers and larger aggregates were observed in Ne matrices, but could only be tentatively assigned.[32] Using supersonic jet spectroscopy, the fluorescence of the ACR dimer was unambiguously detected next to the non-fluorescent monomer.[33] The fluorescence quantum yield of the monomer can be increased in solution by polar solvents or protonation,[34] which is in line with theoretical results.[35] However, the theoretical calculation of the dimer based on force fields and parametrised mean-field methods, which describe the dimer as a head-to-tail structure, does not correspond to the experimental results.[33,36]

In this work, we contribute the previously missing elec-

[a] S. Germer, Dr. O. Hübner, Prof. Dr. H.-J. Himmel*
Inorganic Chemistry
Ruprecht-Karls University Heidelberg
Im Neuenheimer Feld 270, 69120 Heidelberg (Germany)
E-mail: hans-jorg.himmel@aci.uni-heidelberg.de

[b] M. Bauer, Prof. Dr. A. Dreuw
Interdisciplinary Center for Scientific Computing
Ruprecht-Karls University Heidelberg
Im Neuenheimer Feld 205, 69120 Heidelberg (Germany)

https://doi.org/10.26434/chemrxiv-2024-2jwqj **ORCID:** https://orcid.org/0000-0001-8111-3047 Content not peer-reviewed by ChemRxiv. **License:** CC BY-NC-ND 4.0

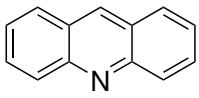

Figure 1. Lewis structure of acridine (ACR) whose isolated dimers and trimers are studied in this work.

tronic absorption spectrum of the ACR monomer isolated in a Ne matrix to the set of spectra already available in literature. This is extended by spectra of the isolated dimer and also the trimer. With the latter, we introduce, for the first time, a method by which larger isolated aggregates can be systematically generated and studied within Ne matrices. This aggregation process is tracked through electronic and vibrational spectra across two spectral ranges. Theoretical calculations explain the shifts observed in these spectra caused by aggregation and provide insight into the underlying photophysics. They also suggest alternative structures of the generated aggregates, which are in agreement with the spectroscopic data.

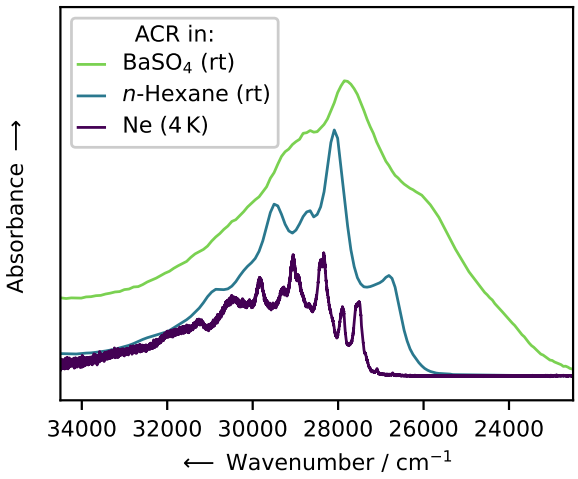

Figure 2. UV/Vis absorbance spectra for ACR in different environments: The solid material in a compressed sample in a $BaSO_4$ matrix (ratio 1:9) at room temperature (green curve), dissolved in *n*-hexane ($25\,\mu mol\,L^{-1}$) at room temperature (blue curve), and the molecules trapped in solid Ne ($100\,\mu m$ thickness) at $4\,K$ (purple curve).

Results and Discussion

The matrix-isolation spectroscopy of Ne matrices provides absorption spectra with small band widths, which is essential for the observation of small aggregates like dimers and trimers. In Figure 2, the influence of the environment on the band width of the electronic absorption spectrum of ACR is demonstrated by comparing different environments of the ACR molecules. The spectrum of the bulk material (solid-state diffuse reflectance measurements on a compressed sample of ACR in a $BaSO_4$ matrix at room temperature) exhibits the broadest bands. The origin of the first electronic excitation is found as a broad shoulder at $26\,200\,cm^{-1}$ with a full width at half maximum (FWHM) of approximately $2000\,cm^{-1}$. In an *n*-hexane solution the spectrum becomes blue-shifted and more resolved (transmittance measurements with a cuvette at room temperature). Here, the origin of the first electronic excitation is located at $26\,810\,cm^{-1}$ and shows a FWHM of around $600\,cm^{-1}$. In a Ne matrix ($100\,\mu m$ thickness) at $4\,K$, it is further blue-shifted by $738\,cm^{-1}$ to $27\,548\,cm^{-1}$, and a FWHM of only $240\,cm^{-1}$ is observed. The Ne solid is the least polarisable of the three environments and therefore has the smallest influence on the electronic excitations. Hence, small changes in the electronic absorption caused by the aggregation of isolated molecules can be studied as shown in the following.

The Acridine Dimer

As already mentioned in the introduction, the formation of aggregates during the deposition of Ne matrices can be promoted by reducing the amount of Ne while keeping the analyte concentration constant. This results in a Ne matrix with a lower layer thickness, which corresponds to a higher concentration. Figure 3a shows the electronic absorption spectra of ACR in solid Ne at $4\,K$ for several matrix concentrations. With thinner, more concentrated matrices, the intensity of the first electronic excitation of monomeric ACR at $27\,548\,cm^{-1}$ decreases. At the same time, two bands become visible at $27\,088$ and $27\,486\,cm^{-1}$. Compared to the first electronic excitation of the monomer, these two bands are red-shifted by 460 and $62\,cm^{-1}$. Since these two bands form with increasing concentration, while the monomer band looses intensity, they are assigned to the ACR dimer. The formation of larger aggregates is unlikely prior to the formation of dimers. The even more red-shifted, weak signals at $26\,818$ and $27\,327\,cm^{-1}$ are then assigned to the ACR trimer, which is discussed in more detail in the second part of this work. Without any Ne, a thin film was obtained whose spectrum resembles the solid-state spectrum in Figure 2.

Further aggregation of guest molecules is also possible after the deposition of a Ne matrix. For this purpose, the respective matrix is annealed to $10\,K$ for $10\,min$. Figure 3b compares the electronic absorption spectra of the Ne matrix with the lowest ACR concentration before and after annealing. The resulting changes in the spectrum correspond to the changes with increasing concentration, confirming the assignment of the dimer bands. Both strategies show that in addition to the first electronic 0-0 transition of the monomer, the other monomer absorptions also change slightly. The bands around $27\,900$, $29\,000$, $30\,500$ and $32\,000\,cm^{-1}$ simultaneously loose intensity. Therefore, these bands are assigned to the vibronic progression of this electronic excitation. The signals around $28\,400$, $29\,800$ and $31\,200\,cm^{-1}$, on the other hand, hardly vary in intensity. Furthermore, the first of these bands, at $28\,370\,cm^{-1}$, is blue-shifted by $70\,cm^{-1}$ to $28\,440\,cm^{-1}$. This implies that this is a second electronic excitation of the ACR monomer, which is less affected by aggregation compared to the first electronic excitation. Accordingly, the blue-shifted band can be assigned to a third electronic 0-0 transition of the ACR dimer. The presence of another excited electronic state close to the first one has already been postulated by Narva et al. using polarised UV absorbance spectra of equally aligned ACR molecules in biphenyl single crystals at $2\,K$.[27] They assigned these two band systems to the $^1A_1$ (Platt's ^1L_a) and the energetically higher $^1B_2$ state (Platt's ^1L_b). Note, that these states can be assigned in a more consistent man-

https://doi.org/10.26434/chemrxiv-2024-2jwqj **ORCID:** https://orcid.org/0000-0001-8111-3047 Content not peer-reviewed by ChemRxiv. **License:** CC BY-NC-ND 4.0

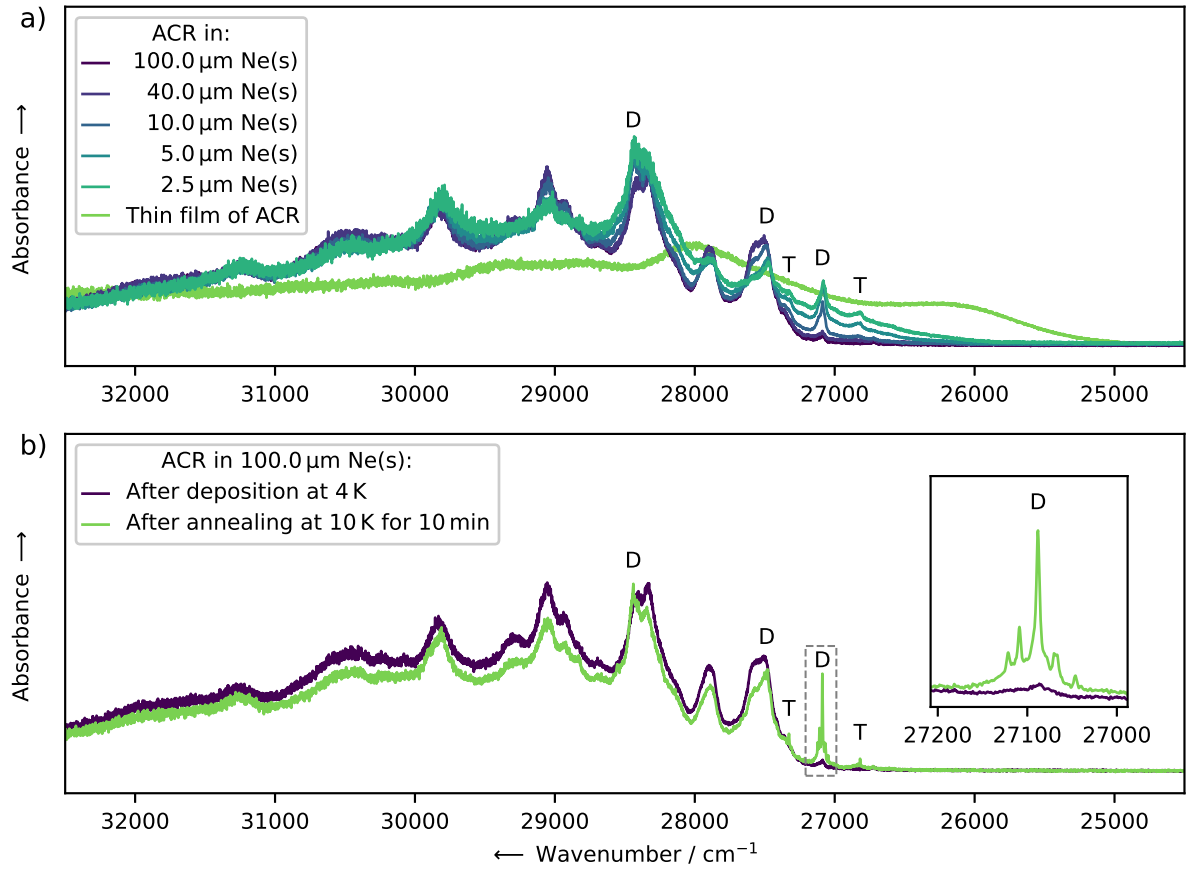

Figure 3. High-resolution electronic absorbance spectra of ACR in solid Ne at 4 K after deposition for 5 min (evaporated at 72 °C and 10^{-6} mbar). a) Spectra recorded for various concentrations (Ne matrix thicknesses between 100 and 2.5 µm) and a thin film of non-diluted solid. b) Spectra recorded for the most diluted Ne matrix (100 µm thickness) before and after annealing to 10 K for 10 min. The D denote bands due to dimers, and the T bands assigned to trimers, which are discussed in detail in the second part of this article.

ner, using ^1L_w and ^1L_s, respectively.[37] However, the energetic splitting between these two states varies with the environment. The smallest splitting of around 820 cm^{-1} is found in Ne at 4 K. It increases to about 1300 cm^{-1} in *n*-hexane solution and is about 2000 cm^{-1} in the solid, in each case at room temperature (cf. Figure 2). In monocrystalline biphenyl matrices at 2 K the value is similar to the pure solid. Since aggregation to the dimer also increases this splitting, it reflects this environmental influence at the molecular level.

The dimer bands differ from those of the monomer not only in their energy, but also in their width. The ACR monomer shows unusually broad bands with a FWHM of more than 150 cm^{-1}, which is described also in the literature for various cases and is particularly evident in direct comparison with the narrower bands in spectra of anthracene.[25,26,32] Calculations have already shown that the excited state with the lowest adiabatic energy difference of ACR is the non-fluorescent $^1B_1$ state with $n\pi^*$ character.[35] Although this state was not accessible by polarised absorption spectroscopy,[27] the broad bands of the other transitions were interpreted as an indirect indication of its presence. The dimer, on the other hand, shows absorption bands with smaller FWHMs of around 50 cm^{-1}. At the lowest matrix concentration, even the underlying fine structure of its first electronic excitation becomes visible, which is highlighted in Figure 3b. In contrast to the usual inhomogeneous line broadening due to a statistical (Gaussian) distribution in the matrix host lattice, homogeneously broadened lines (Lorentzian profile) of individual very similar conformers and/or different matrix sites with FWHMs of 3 to 6 cm^{-1} and line spacings of 10 to 20 cm^{-1} are resolved here. Detailed information on how this was determined can be found in the Supporting Information. Consequently, it can be assumed that the minimum of the low-lying $^1B_1$ state has been raised in energy and the broadening effect in the dimer spectrum has been reduced. This is supported by the fact that a fluorescent dimer has been observed in supersonic jets,[33] which excludes the possibility of a non-fluorescent excited state being the lowest-energy excited state. Furthermore, the supersonic jet dimer exhibited a 0-0 fluorescence transition of 27 018 cm^{-1}, which is very close to but slightly red-shifted (Stokes shift) from the first electronic 0-0 absorption transition of 27 088 cm^{-1} we observe in Ne matrices. This, in turn, supports the assignment of an ACR dimer to the supersonic jet fluorescence spectrum made by Prochorow et al.[33] and disagrees with its reassignment to an ACR-$(H_2O)_2$ aggregate proposed later by Mitsui et al.[38,39]

In order to understand how the photophysics of ACR changes upon aggregation, quantum-chemical calculations were carried out for the monomer and the dimer. First, dimer structures were sampled with different horizontal displacements and torsions between the monomers, yielding the lowest minimum-energy structure. Then, vibrationally

https://doi.org/10.26434/chemrxiv-2024-2jwqj **ORCID:** https://orcid.org/0000-0001-8111-3047 Content not peer-reviewed by ChemRxiv. **License:** CC BY-NC-ND 4.0

resolved electronic absorption spectra were calculated on the basis of this structure. For consistency, the screening procedure as well as the level of theory are exactly the same as in a previously published study.[24]

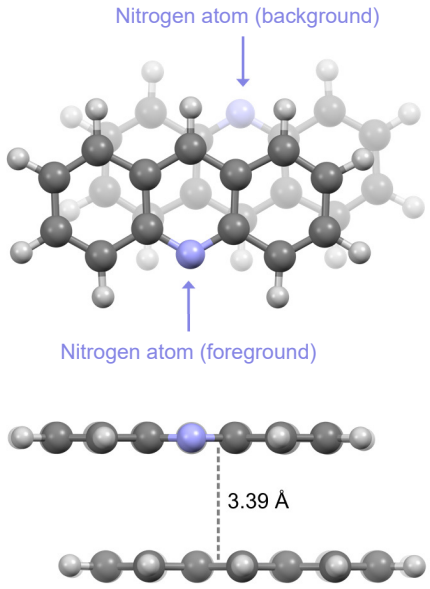

Figure 4. Global minimum-energy structure (C_i-like symmetry) of the ACR dimer calculated at the BHLYP-D3BJ/def2-TZVPP level of theory. The simulated electronic absorption spectrum for this structure is included in Figure 5.

The resulting structure of the most stable ACR dimer exhibits a slip-stacked structure shown in Figure 4. The aromatic planes of the two molecules are co-planar at a distance of 3.39 Å. One of them is rotated by 178° and horizontally displaced by 1.65 Å. This displacement is composed of a component along the short axis of the molecule of 0.98 Å and one along the long axis of 1.33 Å, where the short axis is defined as the normal axis to the picture shown at the bottom of Figure 4, while the long axis is defined as the axis orthogonal to the short axis and the vector defining the distance between both monomers. According to its symmetry, the permanent electric dipole moment of the dimer of 0.02 D is close to zero (monomer: 1.98 D).

This dimer structure was used to simulate a vibrationally resolved electronic absorption spectrum, which is compared to the simulated monomer spectrum and experimental spectra before and after annealing in Figure 5. These simulations were obtained using the independent mode displaced harmonic oscillator, IMDHO,[40,41] model. The energies of the calculated and experimental electronic 0-0 transitions are compared in Table 1. The most remarkable feature in the experimental spectra is that the first electronic excitation from the monomer to the dimer splits into two differently red-shifted excitations. This is well reproduced by the simulation, with deviations of only 40 and 27 cm^{-1} for the $S_{1,D} \leftarrow S_{0,D}$ and $S_{2,D} \leftarrow S_{0,D}$ transitions of the dimer compared to the experiment. The calculated $S_{2,M} \leftarrow S_{0,M}$ transition of the monomer only splits at very short distances, with both resulting transitions being blue-shifted with respect to the corresponding monomer transition. The $S_{6,D} \leftarrow S_{0,D}$ in the dimer is practically dark, which is in line with the experiment, as only one additional peak to the monomer peak is found. The calculated blue-shift of the $S_{5,D} \leftarrow S_{0,D}$ transition is 283 cm^{-1} for the vertical excitation, which deviates by 213 cm^{-1} from the experiment. However, the calculated energy of this second electronic excitation is 3440 cm^{-1} higher than the experimental value, even after applying a shift of 2389 cm^{-1} to align the first vertical excitation of the simulation with the corresponding experimental one. Applying this additional shift can be justified by the fact that high-level calculations on the monomer predict the lowest three singlet excitations to be energetically close to each other.[35] The oscillator strength of the $S_{3,M} \leftarrow S_{0,M}$ transition is two orders of magnitude lower than that of the $S_{1,M} \leftarrow S_{0,M}$ transition, while the $S_{2,M} \leftarrow S_{0,M}$ transition provides an oscillator strength within the same order of magnitude. The vibrational structure of these two electronic excitations then reproduces the experimental monomer spectrum well. The dimer is also detected in the IR spectra, and calculated and observed IR wavenumbers are in good agreement. The IR spectra will be discussed in the section dealing with the trimer.

Table 1. Experimental (Ne matrix, 4 K) and calculated (BHLYP-D3BJ/def2-TZVPP) adiabatic excitation energies of the 0-0 transitions for the two first electronic excitations of the ACR monomer and the corresponding (separated in the table) three excitations of its dimer (in cm^{-1}). The dimer shifts of the dimer excitations are derived therefrom. All calculated energies are red-shifted by 2389 cm^{-1}, which is the inherent error of the applied theoretical method, to align the calculated and experimental monomer 0-0 transition of the $S_{1,M} \leftarrow S_{0,M}$ electronic excitation.

Transition	Energy / cm^{-1}	Dimer shift / cm^{-1}
$S_{1,M} \leftarrow S_{0,M}$ (expt.)	27548	-
$S_{1,M} \leftarrow S_{0,M}$ (calcd.)	27548	-
$S_{1,D} \leftarrow S_{0,D}$ (expt.)	27088	−460
$S_{1,D} \leftarrow S_{0,D}$ (calcd.)	27128	−420
$S_{2,D} \leftarrow S_{0,D}$ (expt.)	27486	−62
$S_{2,D} \leftarrow S_{0,D}$ (calcd.)	27513	−35
$S_{2,M} \leftarrow S_{0,M}$ (expt.)	28370	-
$S_{2,M} \leftarrow S_{0,M}$ (calcd.)	28370[a]	-
$S_{3,D} \leftarrow S_{0,D}$ (expt.)	28440	+70
$S_{3,D} \leftarrow S_{0,D}$ (calcd.)	28663[a,b]	+283[b]

[a] Red-shifted by an additional 3440 cm^{-1} to match the expt. value. [b] Non-adiabatic excitation energy.

Now the question arises about the origin of the splitting of the first electronic excitation of the monomer in the dimer. A common initial assumption is that such a splitting results from Davydov splitting due to the formation of H- or J-aggregates,[42] which can exhibit unusual behaviour.[43,44] But, through the investigation of benzoacridine dimers, we have shown that these dimers do not show Davydov splitting.[24] To better understand the influence of dimerisation in ACR, the energies of the energetically lowest eight electronic singlet excitations of the dimer are calculated at varying distances between the two molecular planes between the equilibrium distance of 3.39 Å and an additional 5.0 Å. This is visualised in Figure 6. As can be seen, $S_{1,M}$ splits into two states at a significantly larger distance than the other excited monomer states. This is due to the fact, that at large distances excitonic coupling dominates the interaction between both monomer states, resulting in symmetric

https://doi.org/10.26434/chemrxiv-2024-2jwqj **ORCID:** https://orcid.org/0000-0001-8111-3047 Content not peer-reviewed by ChemRxiv. **License:** CC BY-NC-ND 4.0

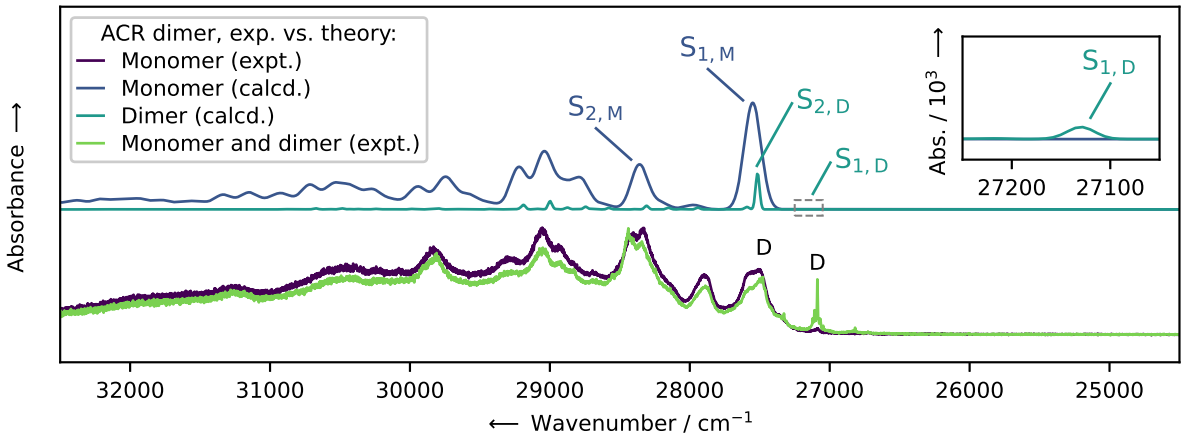

Figure 5. Comparison between the experimental vibrationally resolved electronic absorbance spectra (Ne matrix of $100\,\mu m$ thickness at $4\,K$ after deposition for $5\,min$, with sublimation of ACR at $72\,°C$ and $10^{-6}\,mbar$, and after annealing to $10\,K$ for $10\,min$) and corresponding simulated spectra calculated at the BHLYP-D3BJ/def2-TZVPP level of theory utilizing the IMDHO ansatz. The simulated spectra are red-shifted by $2389\,cm^{-1}$ to align the calculated and experimental 0-0 transition of the monomer $S_{1,M} \leftarrow S_{0,M}$ electronic excitation. The $S_{2,M} \leftarrow S_{0,M}$ is red-shifted by an additional $3440\,cm^{-1}$ to match the experimental spectrum.

splittings proportional to the square of the transition dipole moments. The $S_{1,M} \leftarrow S_{0,M}$ transition possesses a larger transition dipole moment than the other transitions under consideration, exhibiting larger splittings. However, the orbital decomposition is very involved and will therefore be discussed in more detail later. Since $S_{2,M}$ and $S_{3,M}$ possess smaller transition dipole moments, they barely split when approaching the dimer, with again only one state acquiring oscillator strength. The states originating from $S_{2,M}$ and $S_{3,M}$ also take up a blue shift when approaching the dimer, which is experimentally observed for the $S_{2,M}$ state, see Figure 5. Finally the state with the highest energy on the right hand side of Figure 6 drastically changes in energy with varying intermolecular distance. This is due to the fact that it is a charge-transfer (CT) state, which does not appear within the spectral range of the monomer depicted in Figure 5, but it does contribute to the corresponding dimer spectrum. Note however, that DFT is known to underestimate the energy of charge transfer states, even at the given level of Hartree-Fock exchange. Hence, this charge-transfer state, which exhibits a rather small oscillator strength anyway, is not taken into account for the simulated dimer spectrum.

As already mentioned above, the $S_{1,M}$ state splits at large distances and will therefore be discussed in more detail with respect to the dominant orbital contributions of the corresponding excitations. The $S_{1,M} \leftarrow S_{0,M}$ transition is well approximated by the LUMO ← HOMO transition, and the splitted transitions can be decomposed into orbital transitions between the HOMO and LUMO orbitals of both monomers in good approximation as well. The exact contributions are visualised in Figure 7. At an additional $5\,Å$ to the equilibrium dimer distance the orbitals are localised on the corresponding monomer, but both the $S_1 \leftarrow S_0$ and $S_2 \leftarrow S_0$ excitations already consist of almost equal contributions of the LUMO ← HOMO transitions of the corresponding monomers. Pushing both monomers $1\,Å$ closer to each other still yields localised LUMOs, but the HOMOs now start to delocalise over both monomers, and while the $S_1 \leftarrow S_0$ transition barely changes in its decomposition,

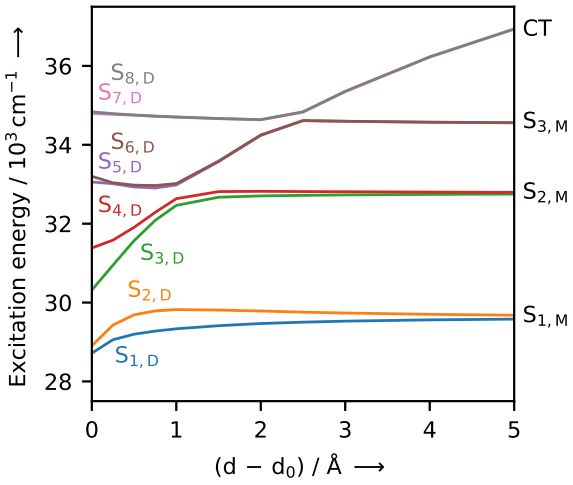

Figure 6. Vertical excitation energies relative to the corresponding ground state are plotted against the distance added to the intermolecular equilibrium distance of the dimer for its energetically lowest 8 excited singlet states, calculated at the BHLYP-D3BJ/def2-TZVPP level of theory.

the $S_2 \leftarrow S_0$ excitation now provides considerable contributions from all four possible orbital transitions. Note, that the character of both states undergoes only minor changes here, as the splitting is still well described by excitonic coupling. At an additional $1.5\,Å$ to the equilibrium dimer distance, the weights barely change for the $S_1 \leftarrow S_0$ transition, since it is build from orbital transitions originating from the LUMO ← HOMO transitions of the corresponding monomers. In this sense the current $S_2 \leftarrow S_0$ transition provides a Dexter-like transition. However, it shall be noted, that the orbitals are now fully delocalised over both fragments, which is why at this distance the system cannot be characterised by two distinct monomers anymore. This becomes more evident at even shorter intermolecular distances, where the average of the energies of both states does not agree with the energy of the $S_{1,M}$ state and the

https://doi.org/10.26434/chemrxiv-2024-2jwqj **ORCID:** https://orcid.org/0000-0001-8111-3047 Content not peer-reviewed by ChemRxiv. **License:** CC BY-NC-ND 4.0

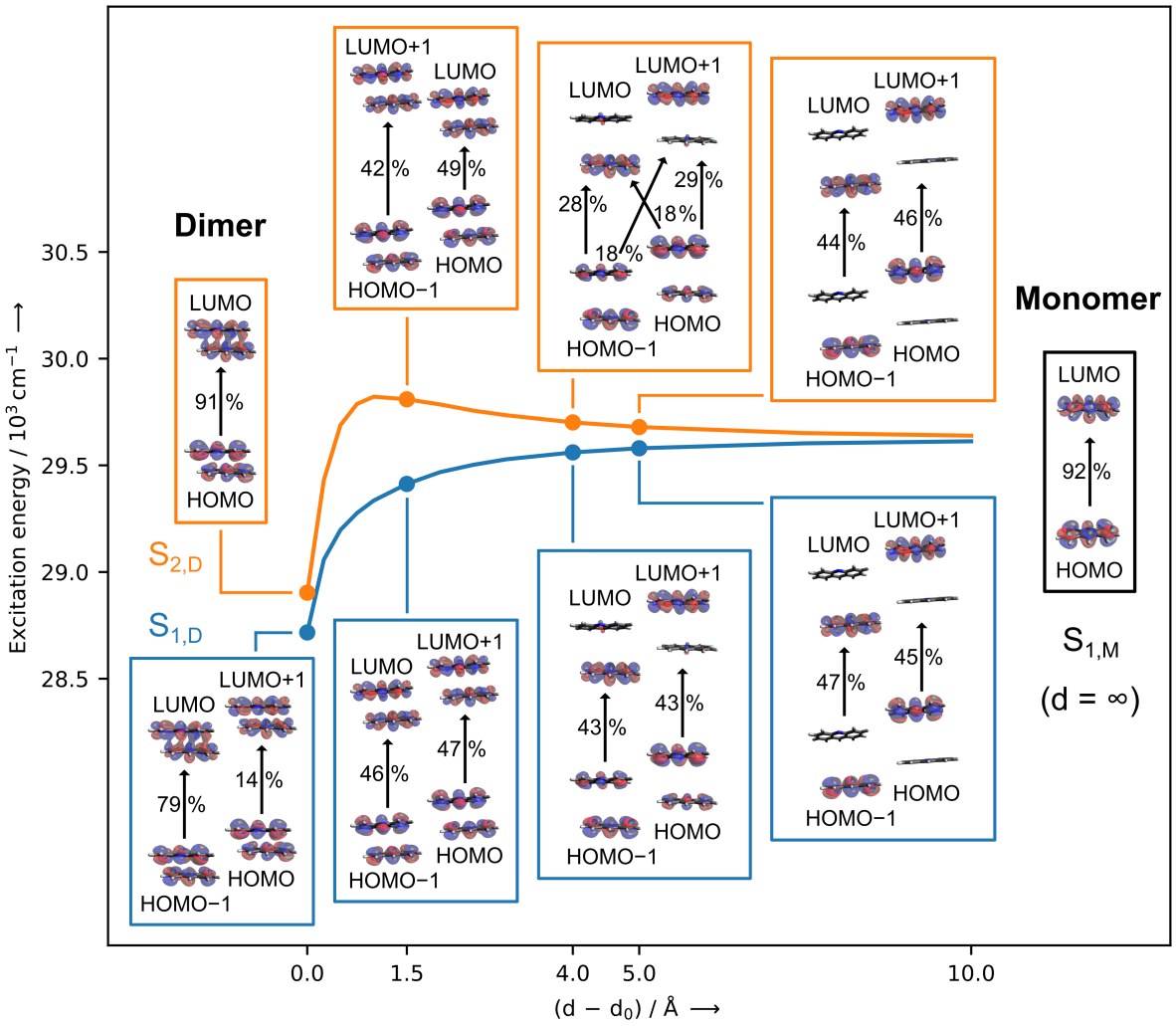

Figure 7. Zoomed in region below $30\,000\,\mathrm{cm}^{-1}$ of Figure 6, with detailed orbital decompositions of the corresponding states depicted at specific intermolecular distances.

orbitals are far from being degenerate. Hence, this is the point, at which the excitonic coupling of the transitions is no dominant but overcompensated by orbital interactions. Finally, both transitions significantly change in character at the equilibrium dimer distance, compared to larger distances. First of all, note that a considerable amount of electron density is now located between both monomers, as can be seen e.g. from the LUMO. Furthermore, the $S_1 \leftarrow S_0$ transition still decomposes into the same orbital transitions, but with different weights, yielding the LUMO ← HOMO-1 transition as the dominant contribution, while the $S_2 \leftarrow S_0$ transition is well approximated by the LUMO ← HOMO transition now.

Due to the good agreement between the experimental and the calculated dimer shifts, the structure of the matrix-isolated ACR dimer is expected to be close to the calculated global minimum-energy structure (Figure 4). Consequently, we disagree with the head-to-tail structure proposed by Prochorow et al.[33,36] It is less supported by experimental results and the applied low-level theoretical methods underestimate dispersion interactions, favouring a structure with a hydrogen bond from the CH hydrogen atom of the central ring of the first molecule to the nitrogen atom of the second one. Dispersion interactions should not be disregarded in general. Even for pyridine, the energy of a slip-stacked structure is comparable to competing structures with hydrogen bonds or a T-shape.[21] With two additional annulated benzene rings, a slip-stacked structure was therefore expected for the ACR dimer. This influence can also be observed in the solid state. Although there are many different polymorphs of the solid ACR,[45] several dimer-like substructures can be recognised that are similar to the isolated dimer and exhibit anti-parallel oriented permanent electric dipole moments (cf. Supporting Information). For benzo[*a*]- and benzo[*c*]acridine, which include an additional benzene ring, the contrast between the isolated and solid-state dimer is already notably more pronounced due to dispersion interactions to surrounding molecules.[24]

The Acridine Trimer

As noted in the first part, two signals in Figure 3 can be attributed to a trimer. This assignment is additionally supported by infrared (IR) absorption spectra. In Figure 8a, it can be observed that the vibrational frequency of $737.3\,\mathrm{cm}^{-1}$ of the ACR monomer shifts both to higher and to lower frequencies as less Ne is used and the matrix concentration is increased. Annealing the most diluted matrix reveals that

https://doi.org/10.26434/chemrxiv-2024-2jwqj **ORCID:** https://orcid.org/0000-0001-8111-3047 Content not peer-reviewed by ChemRxiv. **License:** CC BY-NC-ND 4.0

the band shifted by $1.8\,\mathrm{cm}^{-1}$ to a higher energy statistically forms before the band shifted by $3.5\,\mathrm{cm}^{-1}$ to a lower energy (Figure 8). Therefore, the former can be assigned to the ACR dimer and the latter to the ACR trimer. A total of five vibrations are found that are IR-active possessing sufficient intensities and showing two additional signals with shifts of different signs when aggregation is induced. An additional eight vibrations display a single extra band, each shifted to a higher energy. The vibrational frequencies and their observed experimental aggregate shifts are shown in Table 2. The shifts calculated for the previously discussed dimer structure (Figure 4) are presented for comparison. The experimental and calculated values of the dimer all have a positive sign and exhibit an average deviation of only about $1\,\mathrm{cm}^{-1}$, further confirming the assignment of this structure. It is worth noting that additional signals at slightly higher frequencies have previously been observed in IR spectra of matrix-isolated ACR.[31] However, they were not associated with a dimer in this context.

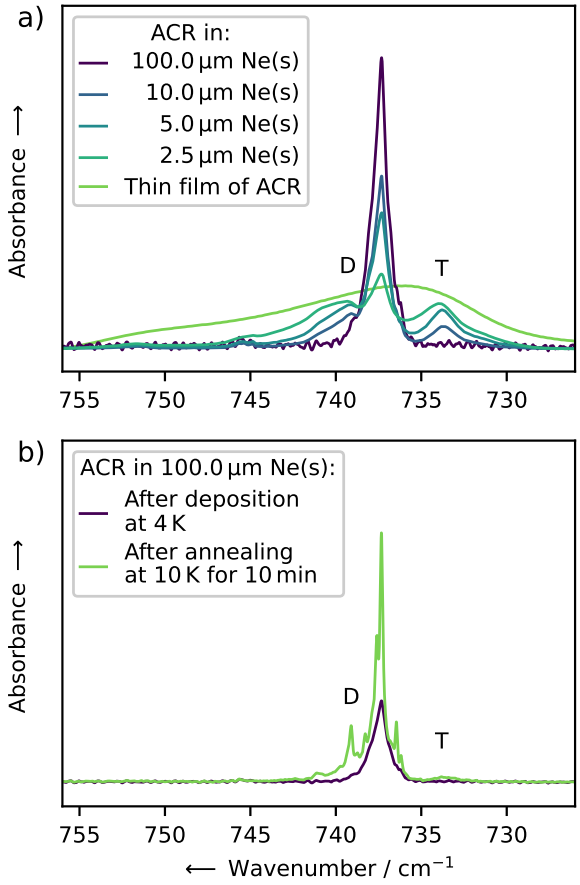

Figure 8. Region around the $737.3\,\mathrm{cm}^{-1}$ signal of the IR absorption spectrum of ACR in solid Ne at $4\,\mathrm{K}$ after deposition (evaporated at $72\,^{\circ}\mathrm{C}$ and $10^{-6}\,\mathrm{mbar}$). a) Spectra recorded for various concentrations (Ne matrix thicknesses between 100 and $2.5\,\mu\mathrm{m}$) and a thin film of non-diluted solid. b) Spectra recorded for the most diluted Ne matrix ($100\,\mu\mathrm{m}$ thickness) before and after annealing to $10\,\mathrm{K}$ for $10\,\mathrm{min}$. "D" and "T" denote dimer and trimer bands, respectively.

Annealing the most diluted matrix is an approach for identifying dimers, as it predominantly promotes the aggregation of monomers, statistically resulting in the formation of dimers. The higher the number of dimers already formed during deposition and present in the matrix alongside monomers, the greater the chance that they will form also trimers during annealing. A strategy for distinctly assigning bands to the trimer is therefore to systematically anneal matrices with higher concentrations, where dimers are present next to monomers. With this method, UV and IR spectra of ACR at different concentrations before and after annealing were recorded, which are reproduced in Figure 9. They show that, through annealing, the bands assigned to the dimer gradually gain less additional intensity as the amount of Ne decreases and the matrix concentration increases. Simultaneously, the bands assigned to the trimer increase more in intensity during annealing. While this is more noticeable from the shifted vibrational frequency than from the electronic excitations, as the latter exhibit a broad background and the relative oscillator strengths of its electronic transitions appear to be lower compared to the mono- and dimer, it is visible in both spectral regions. In the most concentrated matrix, with the minimum amount of Ne ($2.5\,\mu\mathrm{m}$), it is even visible that the increase in the trimer bands during annealing is again less pronounced than at lower concentrations. Although the trimer band intensities increase less, broad backgrounds are formed below it. In the case of the vibrational frequency of $737.3\,\mathrm{cm}^{-1}$, this indicates the formation of larger aggregates than a trimer. This is supported by the fact that in a thin layer of ACR without any Ne, an IR signal with an absorbance maximum between that of the monomer and the trimer is found (Figure 8a). Consequently, signals from aggregates consisting of three and more molecules all show in a confined region around the respective monomer band. However, the first electronic excitation is further red-shifted with each additional molecule in the aggregate. Since an energy difference of around $600\,\mathrm{cm}^{-1}$ remains between the 0-0 transitions of the first electronic excitations of the trimer and the solid (thin film), it can be assumed that aggregates consisting of more than three molecules can be found here (cf. Figure 3a). With the technical possibility to accurately apply even less amounts of Ne to the analyte molecules, such aggregates could be selectively generated and should be experimentally distinguishable, although the vibrational frequencies alone may no longer suffice for this purpose.

With this emerging trend in the formation of larger aggregates and the coincidence of the resulting effects in two different spectral ranges, a trimer is very likely present in the experiment. A consistent computational screening for the ACR trimer structure by quantum-chemical calculations cannot be performed within reasonable computational effort, due to the multitude of possible geometries that need to be sampled. On the other hand, since the most stable dimer structure is known, it can be assumed that the trimer also has a slip-stacked structure, but consists of three parallel molecular planes. The dipole moments of molecules lying directly on top of each other will most likely also align in an antiparallel manner, causing the dipole moment of the central molecule to be oriented in the opposite direction to those of the two outer molecules. When considering the relative shifts, it is crucial to note that during structural optimisation, the molecules in the dimer are displaced relative to each other along the short axis, even from an initial structure where the molecules are directly superimposed in this dimension. Accordingly, no shift is applied along the short axis for the initial structure of the trimer. The displacement along the long axis in the dimer showed that a

https://doi.org/10.26434/chemrxiv-2024-2jwqj ORCID: https://orcid.org/0000-0001-8111-3047 Content not peer-reviewed by ChemRxiv. License: CC BY-NC-ND 4.0

Table 2. Experimental (Ne matrix, 4 K) and calculated (BHLYP-D3BJ/def2-TZVPP) shifts of the vibrational wavenumbers of the ACR dimer and trimer relative to the respective monomer wavenumbers (in cm^{-1}). Only the 13 frequencies at which signals from dimers or trimers were distinguishable in the experiment are listed.

$\widetilde{\nu}_{\mathrm{M}}$ (expt.) / cm^{-1}	$\Delta\widetilde{\nu}_{\mathrm{D}}$ (expt.) / cm^{-1}	$\Delta\widetilde{\nu}_{\mathrm{D}}$ (calcd.) / cm^{-1}	$\Delta\widetilde{\nu}_{\mathrm{T}}$ (expt.) / cm^{-1}	$\Delta\widetilde{\nu}_{\mathrm{T}}$ (calcd.) / cm^{-1}
618.3	+4.1	+0.9	-	+0.9
655.8	+3.0	+1.5	-	+1.6
737.3	+1.8	+2.4	−3.5	−2.8
789.0	+1.3	+1.4	−1.9	−0.5
815.2	+3.8	-	-	-
855.4	+2.1	+1.8	−1.6	−0.9
908.0	+3.9	+4.7	−2.6	+2.0
1000.4	+3.3	-	-	-
1143.3	+7.2	+2.0	-	+1.7
1397.3	+1.4	-	-	-
1405.4	+2.0	-	-	-
1467.8	+1.6	-	−1.3	-
1520.2	+2.6	+1.3	-	+2.0

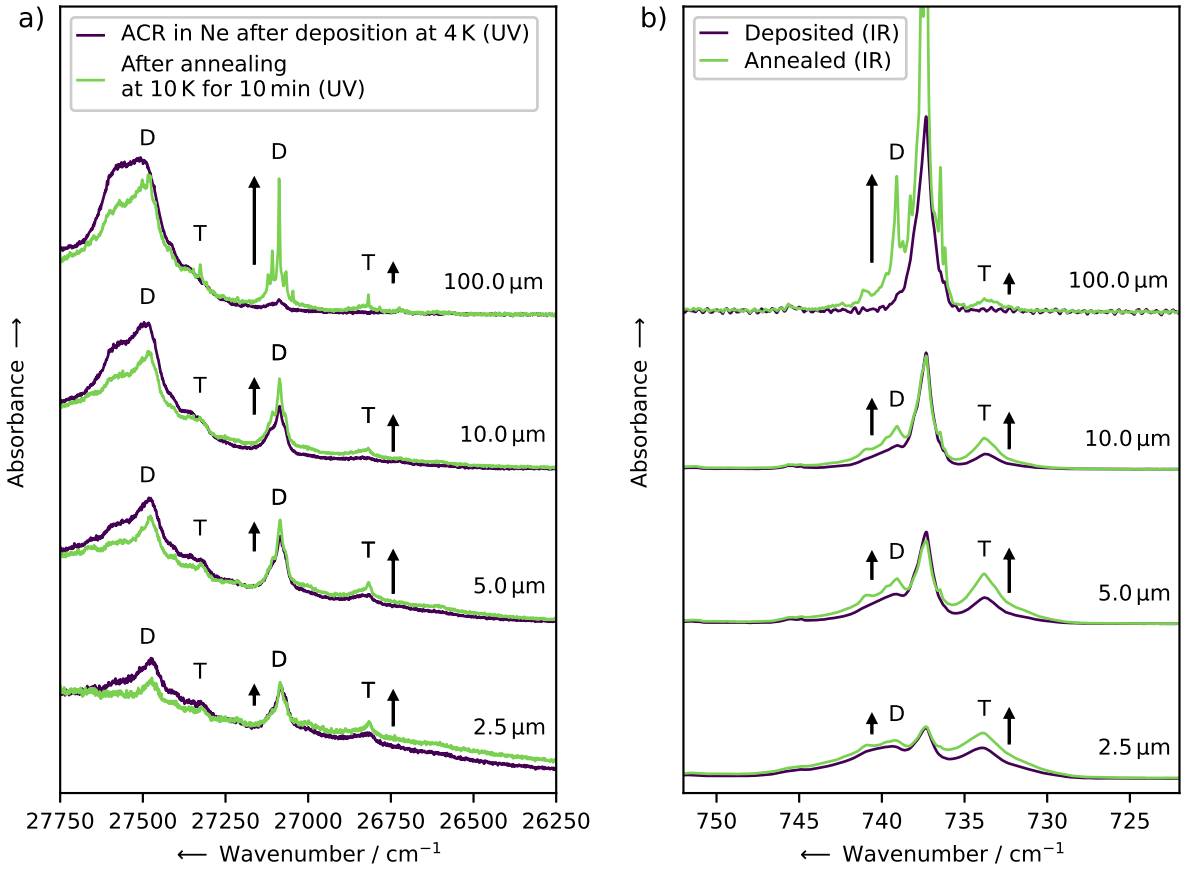

Figure 9. Spectra of ACR aggregates in solid Ne at 4 K after deposition for 5 min (evaporated at 72 °C and 10^{-6} mbar) and annealing to 10 K for 10 min for various concentrations (Ne matrix thicknesses between 100 and 2.5 µm). a) Sections of the electronic excitation spectra. b) Region around the 737.3 cm^{-1} monomer band in the IR spectrum. "D" and "T" denote dimer and trimer bands, respectively.

value of 1.33 Å led to the lowest minimum-energy structure. In the trimer, the third molecule could be shifted in the same or opposite direction along the long axis as the second, middle molecule. Since no reasonable decision can be made in this regard, both were considered. Considering only the upper or the lower dimer in those initial trimer structures, one therefore obtains the initial guess structure that yielded the most stable dimer structure.

https://doi.org/10.26434/chemrxiv-2024-2jwqj **ORCID:** https://orcid.org/0000-0001-8111-3047 Content not peer-reviewed by ChemRxiv. **License:** CC BY-NC-ND 4.0

The optimised structures for these two potential trimers were computed using the same methodology as for the dimer. They exhibit an energy difference of only 0.05 kJ mol^{-1}. Vibrational frequencies and electronic excitations were also calculated for both. The former differ between the two structures by less than 1 cm^{-1}. The sign of the shifts relative to the monomer frequencies remains consistent across all vibrations. The first two electronic excitations of the possible trimer structures also differ by a maximum of 345 cm^{-1}, which, considering the accuracy of the calculation, is not a large deviation. Consequently, both structures exhibit a similar level of agreement with the experimental data. Considering the broadening observed in all spectra upon aggregation, it is conceivable that both conformers are generated during matrix deposition. Particularly for the electronic excitations, however, annealing only yields one sharper band for each trimer signal. Consequently, an isomerisation to the thermodynamically favoured conformer can be expected to take place. This is consistent with the calculated difference of 5 kJ mol^{-1} between the Gibbs free energies of the trimer conformers. Disregarding a potential small energy barrier for isomerisation, annealing at 10 K results in an equilibrium that favours only one trimer structure, which is the one possessing higher symmetry, with the two additional ACR molecules shifted in the same direction along the long axis (Figure 10). Similar to the dimer, the aromatic planes of all three molecules are arranged in a co-planar manner, but at distances of 3.40 Å, which exceed that of the dimer by 0.01 Å. The two outer molecules are rotated by 180° and horizontally displaced by 1.66 Å in opposite directions. Hence, the arrangement of two molecules next to each other in the trimer closely resembles the dimer geometry. With the addition of the third molecule, the trimer exhibits a permanent electric dipole moment of 1.87 D (monomer: 1.98 D).

The shifts of the vibrational frequencies computed for this trimer structure relative to the monomer are presented in Table 2, alongside the experimentally observed ones. As can be seen, the experimentally observed shifts are generally well reproduced by the calculated ones. Note that not all experimentally observed bands could be distinctly assigned to a calculated vibrational mode. Moreover, most of the trimer shifts are estimated to be positive from the calculation. These cannot be distinguished experimentally from the potentially overlapping dimer bands though, which all shift to higher frequencies. As no trimer bands were identified in the experiment for the corresponding signals, this can support the assignment of the considered structure to the experimentally observed trimer, unless they are simply not visible due to low oscillator strengths.

The shifts of the electronic excitations of the experimentally observed and the calculated trimer are shown in Table 3 and the corresponding spectra are visualised in Figure 11. As can be seen, the red shift of the $S_{1,T}$ state is calculated as 990 cm^{-1}, which overestimates the red shift but is in reasonable agreement with the experiment. However, the $S_{2,T}$ state is estimated to provide a blue shift, and is therefore qualitatively wrong. Hence, one might expect the $S_{2,T}$ state in the experimental spectrum to actually originate from the vibrational progression of the $S_{1,T}$ state. Even though this is plausible, the actual reason for this deviation lies most likely in the strong overestimation of the energy of the $S_{2,M}$ state, which contributes to both the $S_{1,T} \leftarrow S_{0,T}$ and the $S_{2,T} \leftarrow S_{0,T}$ transition. Hence, if the energy of the $S_{2,M}$ state would be lower in energy, the $S_{2,T}$ state would be shifted to lower energies too. Due to the energetic vicinity of the $S_{2,T}$ and the experimentally observed $S_{2,M}$ state, this effect can be expected to have a strong impact, yielding an overall red instead of a blue shift for the $S_{2,T}$ state.

Overall, the calculated trimer structure is well supported by the experiment, although higher aggregates can not entirely be ruled out. In contrast to the dimer structure, there is no corresponding structural motif for this trimer structure in the different known ACR solid-state structures.[45] This means that despite dimer-like structural motifs in the solid-state packing, crucial differences are to be expected at the interfaces and surfaces of the solid, where the relative orientation of individual neighbouring molecules is dominated

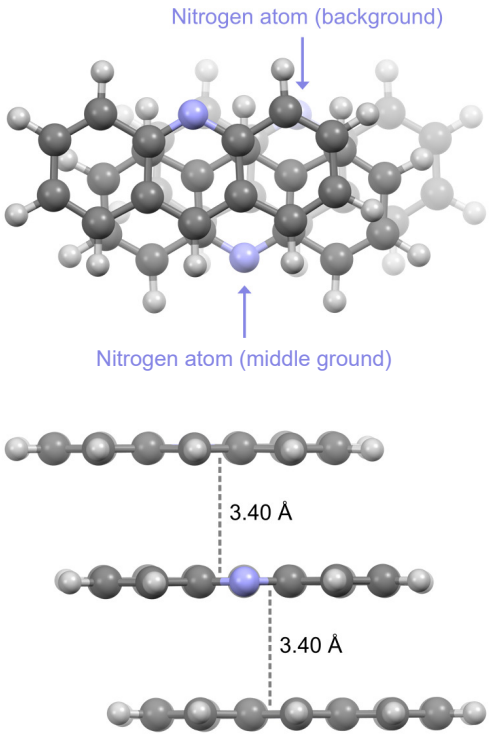

Figure 10. Local minimum-energy structure (C_2-like symmetry) of the proposed ACR trimer. The simulated electronic absorption spectrum for this structure is included in Figure 11.

Table 3. Experimental (Ne matrix, 4 K) and calculated (BHLYP-D3BJ/def2-TZVPP) energies of the 0-0 transitions for the first electronic excitation of the ACR monomer and the first two excitations of its trimer (in cm^{-1}). The trimer shifts of the two trimer excitations are derived therefrom. All calculated energies are red-shifted by 2389 cm^{-1} to align the calculated and experimental monomer 0-0 transition of the $S_{1,M} \leftarrow S_{0,M}$ electronic excitation.

Transition	Energy / cm^{-1}	Trimer shift / cm^{-1}
$S_{1,M} \leftarrow S_{0,M}$ (expt.)	27548	-
$S_{1,M} \leftarrow S_{0,M}$ (calcd.)	27548	-
$S_{1,T} \leftarrow S_{0,T}$ (expt.)	26818	−730
$S_{1,T} \leftarrow S_{0,T}$ (calcd.)	26558	−990
$S_{2,T} \leftarrow S_{0,T}$ (expt.)	27327	−221
$S_{2,T} \leftarrow S_{0,T}$ (calcd.)	27924	+376

https://doi.org/10.26434/chemrxiv-2024-2jwqj **ORCID:** https://orcid.org/0000-0001-8111-3047 Content not peer-reviewed by ChemRxiv. **License:** CC BY-NC-ND 4.0

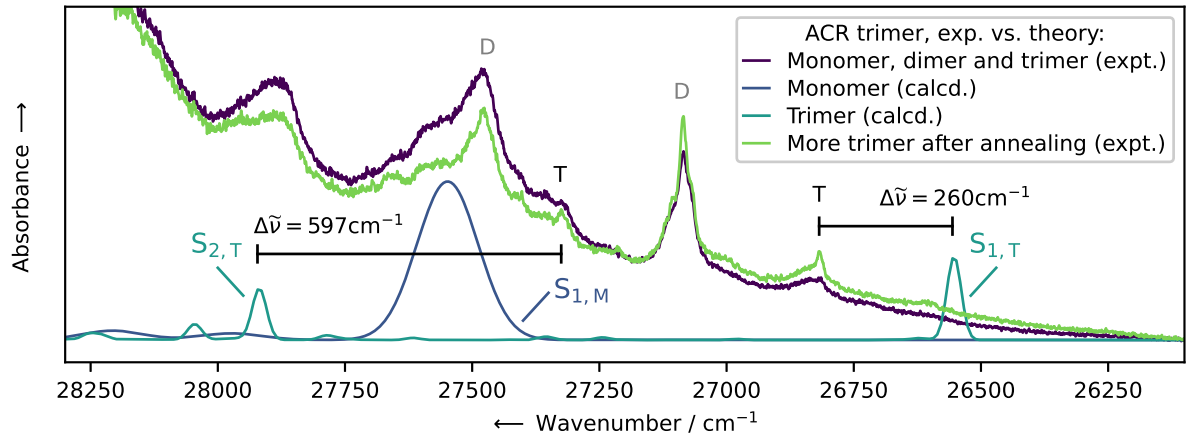

Figure 11. Comparison between the experimental vibrationally resolved electronic absorption spectra (Ne matrix of $5\,\mu m$ thickness at $4\,K$ after deposition for $5\,min$, with sublimation of ACR at $72\,°C$ and $10^{-6}\,mbar$, and after annealing to $10\,K$ for $10\,min$) and corresponding simulated spectra calculated at the BHLYP-D3BJ/def2-TZVPP level of theory utilising the IMDHO approach. The simulated spectra are red-shifted by $2389\,cm^{-1}$ to align the calculated and experimental 0-0 transition of the monomer $S_{1,M} \leftarrow S_{0,M}$ electronic excitation.

less by packing effects and more by individual intermolecular interactions.

Conclusion

To understand intermolecular interactions within molecular aggregates, it is imperative to generate and study such species experimentally. In this work, we achieve this for the first time with the dimer and also the trimer of acridine (ACR) using matrix-isolation spectroscopy. Quantum-chemical calculations facilitate an interpretation of the spectra, by assigning spectroscopic features to specific geometric structures and by identifying peculiar photophysics of these aggregates.

Changes in the electronic structure of ACR upon dimerisation were spectroscopically observed by complementary concentration and annealing experiments in Ne matrices. Such an aggregation process was followed for the first time in two spectral regions, namely by vibrational and electronic absorption spectroscopy. The experimental data support a previous assignment of a dimer detected in supersonic jets. Theoretical calculations following the methodology of a previous study provide a global minimum-energy structure for the dimer. The agreement between experimental and calculated vibrational frequencies and electronic excitations confirms the assignment of this structure. The aggregation leads to a striking splitting of the first electronic excitation of the monomer. Calculations on dimers at slightly larger intermolecular distances reveal a complex alteration of the states, leading to a splitting originatiting from a combination of Davydov splitting and orbital interactions. These dimer excitations are not influenced by a low-lying $n\pi^*$ state like the monomer. The fact that this changes upon aggregation can be of great interest to many research areas when modelling electronic structures of NHPs and considering them for applications in organic electronics.

We also present the first example of a systematic experimental approach to generate larger aggregates such as trimers using the matrix-isolation technique. A combination of concentration and annealing experiments enables a controlled stepwise aggregation. Based on the obtained spectra, theoretical calculations provide a reasonable structure for the observed trimer. It deviates significantly from all structural motifs found in the solid state of ACR and therefore indicates how large the structure differences at interfaces and surfaces can possibly become compared to the crystalline phase of solids.

Our results are a proof of principle of how self-assembled molecular aggregates larger than dimers can be studied by matrix-isolation spectroscopy. In the future, improved experimental setups, enabling higher analyte to Ne ratios during matrix deposition, will allow the controlled generation and characterisation of aggregates larger than those presented here. This could provide unique insights into how thin films grow from one molecule to a macroscopic layer during deposition from the gas phase, which would be of great importance for material sciences.

Supporting Information

The authors have cited additional references within the Supporting Information.[46–48]

Acknowledgements

The authors gratefully acknowledge continuous financial support by the Deutsche Forschungsgemeinschaft (DFG) through projects B01 and B03 within the SFB 1249. For computational resources, we thank the state of Baden-Württemberg for the bwHPC system (JUSTUS 2). Open Access funding enabled and organised by Projekt DEAL.

Conflict of Interest

The authors declare no conflict of interest.

Keywords: acridine • aggregation • electronic excitation • IR spectroscopy • matrix isolation

https://doi.org/10.26434/chemrxiv-2024-2jwqj **ORCID:** https://orcid.org/0000-0001-8111-3047 Content not peer-reviewed by ChemRxiv. **License:** CC BY-NC-ND 4.0

References

[1] H. Ichikawa, R. R. Navarro, Y. Iimura, K. Tatsumi, *Chemosphere* **2010**, *80*, 866.
[2] E. A. Meyer, R. K. Castellano, F. Diederich, *Angew. Chem. Int. Ed.* **2003**, *42*, 1210.
[3] J. L. Brédas, D. Beljonne, V. Coropceanu, J. Cornil, *Chem. Rev.* **2004**, *104*, 4971.
[4] M. O. Sinnokrot, E. F. Valeev, C. D. Sherrill, *J. Am. Chem. Soc.* **2002**, *124*, 10887.
[5] S. Tsuzuki, K. Honda, T. Uchimaru, M. Mikami, *J. Chem. Phys.* **2004**, *120*, 647.
[6] R. Podeszwa, K. Szalewicz, *Phys. Chem. Chem. Phys.* **2008**, *10*, 2735.
[7] J. M. Hayes, *Chem. Rev.* **1987**, *87*, 745.
[8] K. O. Börnsen, H. L. Selzle, E. W. Schlag, *Z. Naturforsch. A* **1984**, *39*, 1255.
[9] H. Saigusa, S. Sun, E. C. Lim, *J. Phys. Chem.* **1992**, *96*, 2083.
[10] G. Rosenblum, Y. Karni, S. Speiser, *Isr. J. Chem.* **1997**, *37*, 445.
[11] T. Forsting, J. Zischang, M. A. Suhm, M. Eckhoff, B. Schröder, R. A. Mata, *Phys. Chem. Chem. Phys.* **2019**, *21*, 5989.
[12] S. Oswald, M. A. Suhm, S. Coussan, *Phys. Chem. Chem. Phys.* **2019**, *21*, 1277.
[13] J. Y. Feng, Y. P. Lee, C. Y. Zhu, P. J. Hsu, J. L. Kuo, T. Ebata, *Phys. Chem. Chem. Phys.* **2020**, *22*, 21520.
[14] F. Sturm, L. N. Philipp, M. Flock, I. Fischer, R. Mitric, *J. Phys. Chem. A* **2024**, *128*, 1250.
[15] P. Benharash, M. J. Gleason, P. M. Felker, *J. Phys. Chem. A* **1999**, *103*, 1442.
[16] T. M. Halasinski, D. M. Hudgins, F. Salama, L. J. Allamandola, T. Bally, *J. Phys. Chem. A* **2000**, *104*, 7484.
[17] H. F. Bettinger, R. Mondal, D. C. Neckers, *Chem. Commun.* **2007**, page 5209.
[18] R. Mondal, C. Tönshoff, D. Khon, D. C. Neckers, H. F. Bettinger, *J. Am. Chem. Soc.* **2009**, *131*, 14281.
[19] C. Tönshoff, H. F. Bettinger, *Angew. Chem. Int. Ed.* **2010**, *49*, 4125.
[20] C. Tönshoff, H. F. Bettinger, *Chem. Eur. J.* **2012**, *18*, 1789.
[21] O. Hübner, J. Thusek, H.-J. Himmel, *Angew. Chem. Int. Ed.* **2023**, *62*.
[22] J. Thusek, M. Hoffmann, O. Hübner, O. Tverskoy, U. H. F. Bunz, A. Dreuw, H.-J. Himmel, *Chem. Eur. J.* **2019**, *25*, 15147.
[23] J. Thusek, M. Hoffmann, O. Hübner, S. Germer, H. Hoffmann, J. Freudenberg, U. H. F. Bunz, A. Dreuw, H.-J. Himmel, *Chem. Eur. J.* **2021**, *27*, 2072.
[24] S. Germer, M. Bauer, O. Hübner, R. Marten, A. Dreuw, H.-J. Himmel, *Chem. Eur. J.* **2023**, *29*, e202302296.
[25] R. M. Macnab, K. Sauer, *J. Chem. Phys.* **1970**, *53*, 2805.
[26] O. Morawski, J. Prochorow, *Chem. Phys. Lett.* **1995**, *242*, 253.
[27] D. L. Narva, D. S. McClure, *Chem. Phys.* **1981**, *56*, 167.
[28] M. B. Mitchell, G. R. Smith, K. Jansen, W. Guillory, *Chem. Phys. Lett.* **1979**, *63*, 475.
[29] M. B. Mitchell, G. R. Smith, W. A. Guillory, *J. Chem. Phys.* **1981**, *75*, 44.
[30] A. L. Mattioda, L. Rutter, J. Parkhill, M. Head-Gordon, T. J. Lee, L. J. Allamandola, *Astrophys. J.* **2008**, *680*, 1243.
[31] A. Mattioda, C. Bauschlicher, A. Ricca, J. Bregman, D. Hudgins, L. Allamandola, *Spectrochim. Acta A* **2017**, *181*, 286.
[32] J. Prochorow, B. Kozankiewicz, B. B. D. Gemi, O. Morawski, *Acta Phys. Pol. A* **1998**, *94*, 749.
[33] J. Prochorow, I. Deperasińska, O. Morawski, *Chem. Phys. Lett.* **2000**, *316*, 24.
[34] L. A. Diverdi, M. R. Topp, *J. Phys. Chem.* **1984**, *88*, 3447.
[35] O. Rubio-Pons, L. Serrano-Andrés, M. Merchán, *J. Phys. Chem. A* **2001**, *105*, 9664.
[36] J. Prochorow, I. Deperasińska, O. Morawski, *J. Mol. Struct.* **2000**, *555*, 97.
[37] M. Hoffmann, S. A. Mewes, S. Wieland, C. Popp, A. Dreuw, *J. Phys. Chem. Lett.* **2019**, *10*, 6112.
[38] C. Harthcock, J. Zhang, W. Kong, M. Mitsui, Y. Ohshima, *J. Chem. Phys.* **2017**, *146*, 134311.
[39] M. Mitsui, Y. Ohshima, S. I. Ishiuchi, M. Sakai, M. Fujii, *Chem. Phys. Lett.* **2000**, *317*, 211.
[40] D. C. Blazej, W. L. Peticolas, *J. Chem. Phys.* **1980**, *72*, 3134.
[41] F. Santoro, C. Cappelli, V. Barone, *J. Chem. Theory Comput.* **2011**, *7*, 1824.
[42] N. J. Hestand, F. C. Spano, *Chem. Rev.* **2018**, *118*, 7069.
[43] C. Zheng, C. Zhong, C. J. Collison, F. C. Spano, *J. Phys. Chem. C* **2019**, *123*, 3203.
[44] C. Zhong, D. Bialas, C. J. Collison, F. C. Spano, *J. Phys. Chem. C* **2019**, *123*, 18734.
[45] E. Schur, J. Bernstein, L. S. Price, R. Guo, S. L. Price, S. H. Lapidus, P. W. Stephens, *Cryst. Growth Des.* **2019**, *19*, 4884.
[46] R. B. Randall, *Mech. Syst. Signal Process.* **2017**, *97*, 3.
[47] X. Mei, C. Wolf, *Cryst. Growth Des.* **2004**, *4*, 1099.
[48] T. Petrenko, F. Neese, *J. Chem. Phys.* **2012**, *137*, 234107.

https://doi.org/10.26434/chemrxiv-2024-2jwqj **ORCID:** https://orcid.org/0000-0001-8111-3047 Content not peer-reviewed by ChemRxiv. **License:** CC BY-NC-ND 4.0

Entry for the Table of Contents

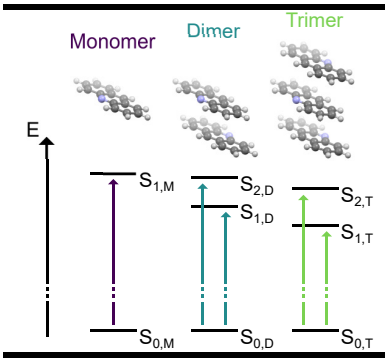

The stepwise aggregation of acridine isolated in solid neon is monitored using IR and UV spectroscopy. A theoretical study provides meaningful structures and insight into the special photophysics of the aggregates.

https://doi.org/10.26434/chemrxiv-2024-2jwqj **ORCID:** https://orcid.org/0000-0001-8111-3047 Content not peer-reviewed by ChemRxiv. **License:** CC BY-NC-ND 4.0